12th International Symposium on Turbulence and Shear Flow Phenomena (TSFP12)
Osaka, Japan (Online), July 19-22, 2022

LARGE-EDDY SIMULATION OF FREE-SURFACE TURBULENT CHANNEL FLOW OVER SQUARE BARS

Razieh Jalalabadi
Civil, Environmental and Geomatic Engineering
University College London
London, WC1E 6BT, UK
r.jalalabadi@ucl.ac.uk

Thorsten Stoesser
Civil, Environmental and Geomatic Engineering
University College London
London, WC1E 6BT, UK
emailt.stoesser@ucl.ac.uk

ABSTRACT

Large-eddy simulations of free surface turbulent channel flow over spanwise-aligned square bars with transitional and *k*-type spacing are performed. Differences in the sign of spatial and temporal velocity fluctuations entail sweep and ejection events which contribute to the dispersive and Reynolds shear stress only in flow over *k*-type roughness. The pressure-strain and transport terms are the dominant components in the budget of the dispersive and double-averaged Reynolds shear stress while the other terms are negligible. Pressure has the largest contribution in the transport of these stresses. Investigating the budgets of wake and double-averaged turbulent kinetic energy reveals that the dominant terms contributing to the generation and fate of these energies are production, transport and convection. Water surface deformations have non-negligible effects in the transport and convection of these stresses and energies.

INTRODUCTION

Turbulent open channel flows over rough surfaces are of fundamental importance as the interaction of bed, bulk flow and water surface influences the flow structure and water surface configuration. Better understanding of the hydrodynamics of this flow type leads to significant improvements in analysing free-surface flows in nature, like river flows, or in predicting floods, respectively. In shallow flows the bed roughness alters the bulk flow structure and water surface directly and the roughness topography plays a crucial role.

Square bars perpendicular to the main flow direction, a canonical and rather simple geometry (Djenidi *et al.*, 1999; Jiminez, 2004) have been applied in numerous researches with the aim to study principle effects of surface roughness on flow characteristics. The main two types of this roughness are *d*-type and *k*-type based on the bar spacing. In *d*-type roughness a stable vortex is formed between the bars while in the *k*-type roughness the flow reattaches to the bed at downstream of bar. The transition from *d*-type to *k*-type roughness occurs at $\lambda/k = 4-5$ where λ is the bar spacing and k is the bar height (Jiminez, 2004). The effects of bed roughness on the averaged parameters can be represented using the double averaging method (Raupach & Shaw, 1982). In double-averaged Navier-Stokes equations new terms known as dispersive shear stresses emerge which represent the spatial variation of time-averaged quantities. All spatial variations of first and second order statistics are induced by near-bed flow heterogeneity and secondary currents when it is present. In flow over rough bed wake kinetic energy (WKE), calculated using the spatial variations of mean velocities, constitute one component of total kinetic energy along with turbulent and mean kinetic energy (TKE and MKE respectively). The spatial variations of mean flow variables are generally small compared to time-averaged variables; however, for some rough surfaces they can contribute to flow dynamics substantially.

Considering the significant effects of geometrical surface parameters on the distribution of first and second order statistics and flow structures (Jalalabadi *et al.*, 2017), the normal and shear stresses and kinetics energies for free-surface turbulent channel flow over spanwise-aligned square bars are investigated based on results of large-eddy simulation of flow over a transitional and a *k*-type roughness at constant Reynolds and Froude numbers. The distributions of mean stresses and kinetic energies present the effects of water surface deformations induced by bed roughness on these flow variables. Quadrant analysis is applied to reveal the contribution of different flow movements on dispersive and Reynolds shear stresses. Shear stress and kinetic energy budgets are scrutinized to explore their dependency on bed roughness and water surface deformations. The remainder of this paper includes numerical simulations, result and discussion and conclusions sections.

NUMERICAL SIMULATIONS

The in-house LES code Hydro3D is employed which has been validated for a large number of flows with similar complexity (Kara *et al.*, 2015; McSherry *et al.*, 2018). The code solves the spatially filtered Navier-Stokes equations

$$\nabla \cdot \mathbf{u} = 0 \qquad (1)$$

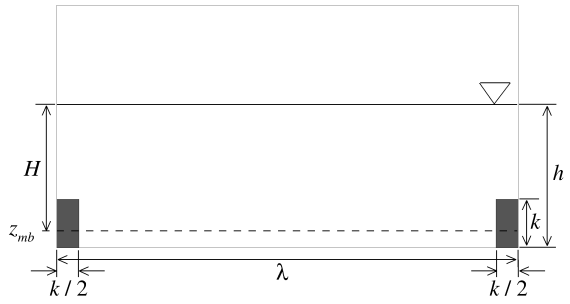

Figure 1. Schematic of the computational domain.

$$\frac{\partial \mathbf{u}}{\partial t} + \mathbf{u}\cdot\nabla\mathbf{u} = -\nabla p + \frac{1}{Re}\nabla^2\mathbf{u} - \nabla\cdot\tau \tag{2}$$

where $\mathbf{u} = (u, v, w)$ is the velocity vector with the components in the streamwise (x), spanwise (y) and wall-normal (z) directions, p is the pressure and τ is the subgrid scale stress tensor. A fractional-step method is applied on a staggered Cartesian grid where in the predictor step a second order Runge-Kutta scheme is applied to predict the velocities. In the corrector step the pressure Poisson equation is solved using a multi-grid method to achieve a divergent flow field. The diffusive terms are computed using second order finite difference scheme and the convective terms are computed using a fifth-order weighted, essentially non-oscillatory (WENO) scheme (Kara *et al.*, 2015). The Wall-Adapting Local Eddy-viscosity (WALE) model is used to calculate eddy viscosity (Nicoud & Ducros, 1999). The free surface is captured using the Level Set Method (Sethian & Smereka, 2003). In this method the interface is tracked by solving a pure advection equation for a level set signed distance function which is zero at the phase interface, negative in air and positive in water. Figure 1 presents the schematic of the computational domain. The domain size for both geometries is $10.4k\times5k\times5k$ in the x, y and z directions respectively. Table 1 provides hydraulic parameters of the simulations. Reynolds and Froude number are calculated using bulk velocity U_b and mean flow depth H. The superscript + represents the inner-scaled quantities calculated using the friction velocity. Periodic boundary condition is applied in the streamwise and spanwise directions. The governing equations are solved via parallel computing using Message Passing Interface (MPI) and the present simulations were validated rigorously in Jalalabadi *et al.* (2021).

Table 1. Hydraulic conditions and grid resolution.

λ/k	H/k	U_b	Re	Fr	Δx^+,Δy^+,Δz^+
5.2	2.5	0.24	7.2×10^3	0.44	4.0,4.7,2.5
10.4	2.5	0.23	8.0×10^3	0.39	3.9,4.6,2.5

RESULTS AND DISCUSSION

Figure 2 shows vertical profiles of spanwise averaged root-mean-square (rms) velocity fluctuations, Reynolds shear stress and turbulent kinetic energy along with spatial fluctuations of velocities, dispersive shear stress and wake kinetic energy to investigate the effects of bars and water surface deformations on these flow variables. The dispersive shear stress is calculated as (Jelly & Busse, 2018)

$$\tilde{u}\tilde{w} = (\overline{u} - \langle\overline{u}\rangle)(\overline{w} - \langle\overline{w}\rangle) \tag{3}$$

where each parentheses on the right hand side represents the spatial fluctuation of a velocity component. Under the bar crest all rms velocity fluctuations, Reynolds shear stress and turbulent kinetic energy are larger in flow over $\lambda/k = 10.4$ than those in $\lambda/k = 5.2$ case. Above the bar crest, only wall-normal rms velocity is slightly larger for $\lambda/k = 10.4$. The peak for $\langle u_{rms}\rangle^+$ under the water surface in flow over $\lambda/k = 10.4$ represents the effects of the large water surface deformation as this peak is not noticeable for flow over $\lambda/k = 5.2$. Similar values for the peak of $\langle v_{rms}\rangle^+$ under water surface in both geometries reveal that only the water surface presence contribute to the generation of this peak regardless of its specific deformations. The wall-normal velocity experiences a weak local increase under the water surface only in $\lambda/k = 10.4$ case. The Reynolds shear stress is similar in both geometries except near the water surface. The strong positive peak of $\langle u'w'\rangle^+$ under the water surface in flow over $\lambda/k = 10.4$ is the effect of the standing wave which is absent in flow over $\lambda/k = 5.2$ (Jalalabadi & Stoesser, 2022*b*). The strong peak of TKE under the water surface is similar to the peak in $\langle u_{rms}\rangle^+$ in that area. $\langle\widetilde{u}\rangle^+$ in flow over both bar spacings has similar values except at the bar crest and under the water surface. At the bar crest $\langle\widetilde{u}\rangle^+$ is larger in flow over $\lambda/k = 5.2$ as, due to the formation of stable vortex between the bars, a significant momentum transfer occurs at the bar crest in this geometry while in flow over $\lambda/k = 10.4$ the momentum transfer is large between the flow everywhere under and above the bar crest. Under the water surface the standing wave causes large spatial variations in the streamwise velocity in flow over larger bar spacing. $\langle\widetilde{v}\rangle^+$ and $\langle\widetilde{w}\rangle^+$ are negligible everywhere except close to the water surface where only $\langle\widetilde{w}\rangle^+$ experiences a weak local increase in flow over $\lambda/k = 10.4$. Dispersive shear stress is similar for both roughness spacing under the bar crest but larger for flow over $\lambda/k = 10.4$ above that height. The peak under the water surface for $\langle\widetilde{u}\widetilde{w}\rangle^+$ has the opposite sign of $\langle u'w'\rangle^+$. Unlike other variable in figure 2, WKE is larger at all wall-normal locations in flow over $\lambda/k = 10.4$ than in flow over $\lambda/k = 5.2$ and reaches its maximum value at the free surface similar to $\langle\widetilde{u}\rangle^+$.

The contribution of velocity fluctuations to the generation of Reynolds and dispersive shear stresses are shown in figure 3. These stresses are divided into four events, Q1 to Q4, based on the sign of their fluctuating components (Wallace, 2016). The second and forth quadrants, $Q2^+$ and $Q4^+$, correspond to vertical flow away from the wall ($w' > 0$) at low speed ($u' < 0$) and towards the wall ($w' < 0$) at high speed ($u' > 0$) and known as ejection and sweep events respectively. As shown in figure 3, $Q2^+$ and $Q4^+$ are the dominant events in both geometries and shear stresses. For the Reynolds shear stress in both geometries, $Q4^+$ is the strongest under the bar crest height while $Q2^+$ is the strongest above that. This is reversed for the dispersive shear stress in flow over $\lambda/k = 10.4$. This reveals that the sign of spatial fluctuations of streamwise and wall-normal velocities are opposite of the sign of temporal fluctuations of these components. The negligible value of all quadrants of the dispersive shear stress in the flow over $\lambda/k = 5.2$ is due to small spatial fluctuations of velocities in this case. The stand-

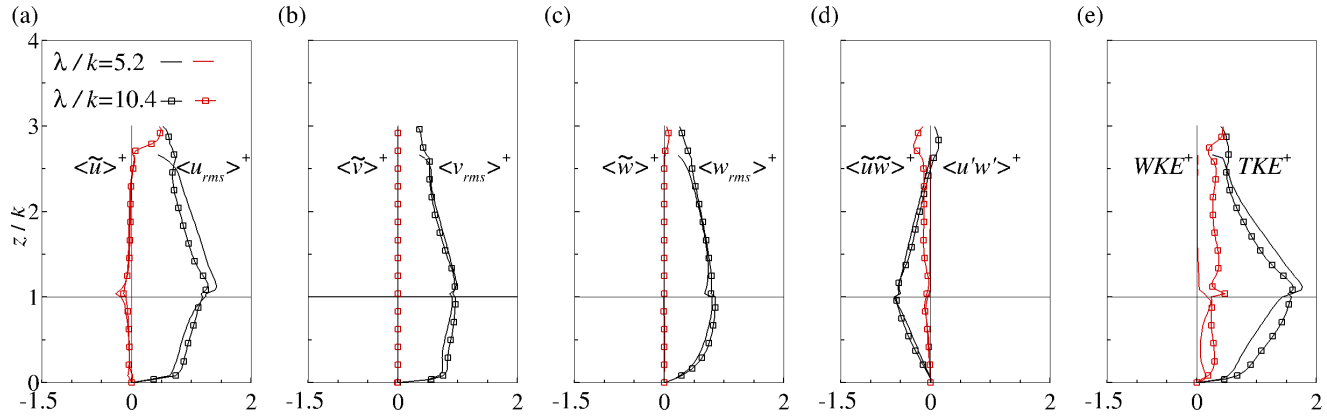

Figure 2. Spatially-averaged (a) streamwise (b) spanwise (c) wall-normal RMS and dispersive velocity fluctuations, (d) Reynolds and dispersive shear stress and (e) turbulent and wake kinetic energy.

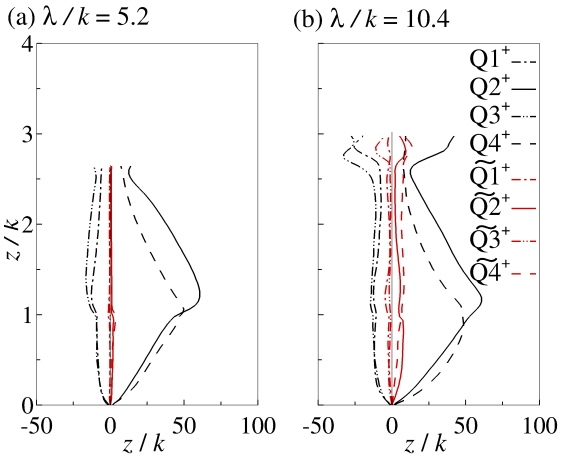

Figure 3. Quadrant components of Reynolds (black) and dispersive (red) shear stress for (a) /k = 5.2 and (b) /k = 10.4.

ing wave at the water surface contributes to the increase in $Q1^+$ to $Q4^+$ under the water surface for $\lambda/k = 10.4$ while in flow over $\lambda/k = 5.2$ this increase is mild. The budgets of dispersive and double-averaged Reynolds shear stress and wake and double-averaged turbulent kinetic energy will be shown to discuss the dominant terms contributing to these second order statistics and explore how they depends on roughness spacing and water surface deformations.

Dispersive and Double-Averaged Reynolds Shear Stress Budget

Figure 4 presents the budgets of the dispersive shear stress calculated using equation (4) for i =1 and k =3 for both bar spacings. All terms in this section are normalized by $H/u_\tau{}^3$. In both cases the production (P), dissipation (ε) and convection (C) terms are negligible and not shown while the pressure-strain correlation (PSC) term is counterbalanced by the transport (T) term. In both geometries PSC is large near the bed consistent with relatively large variations of $\langle\widetilde{u}\rangle^+$ under the bar crest (figure 2(a)). On the vertical face of the bars, PSC is larger in flow over $\lambda/k = 5.2$. This is attributed to the large spatial fluctuations of the mean pressure (Jalalabadi & Stoesser, 2022*a*) due to presence of stable vortex in the cavity between the bars. Absence of this stable vortex in flow over $\lambda/k = 10.4$ leads to the larger interaction of flow above and under the bar crest while in this case PSC is large over the bar due to the larger form drag and gradient of dispersive velocities induced by the bars. The standing wave induces large gradient of dispersive velocities (figure 2(a,c)) which results in a local peak in PSC under the water surface in figure 4(b). The transport term T shown in figure 2(c,d) are generated mainly by pressure transport and other terms are negligible. In flow over $\lambda/k = 5.2$, T is large only under the bar crest and negligible above that implying that only bed roughness contribute to the transport of dispersive shear stress. In larger bar spacing, on the other hand, both bars and water surface contribute to the transport of dispersive shear stress.

$$\frac{\partial <\widetilde{u_i}\widetilde{u_k}>}{\partial t} = \left[-\langle\overline{u_j}\rangle\frac{\partial <\widetilde{u_i}\widetilde{u_k}>}{\partial x_j}\right]_C + \left[-<\widetilde{u_k}\widetilde{u_j}>\frac{\partial\langle\overline{u_i}\rangle}{\partial x_j} - <\widetilde{u_i}\widetilde{u_j}>\frac{\partial\langle\overline{u_k}\rangle}{\partial x_j} + <\widetilde{u_i'u_j'}\frac{\partial\widetilde{u_k}}{\partial x_j}> + <\widetilde{u_k'u_j'}\frac{\partial\widetilde{u_i}}{\partial x_j}>\right]_P + \left[-2\nu<\frac{\partial\widetilde{u_i}}{\partial x_j}\frac{\partial\widetilde{u_k}}{\partial x_j}>\right]_\varepsilon + \left[\frac{1}{\rho}(<\widetilde{p}\frac{\partial\widetilde{u_k}}{\partial x_i}> + <\widetilde{p}\frac{\partial\widetilde{u_i}}{\partial x_k}>)\right]_{PSC} + \left[-\frac{\partial <\widetilde{u_i}\widetilde{u_j}\widetilde{u_k}>}{\partial x_j} - <\frac{\partial\widetilde{u_i'u_j'}\widetilde{u_k}}{\partial x_j}> - <\frac{\partial\widetilde{u_k'u_j'}\widetilde{u_i}}{\partial x_j}> - \frac{1}{\rho}(\frac{\partial\widetilde{p}\widetilde{u_k}}{\partial x_i} + \frac{\partial\widetilde{p}\widetilde{u_i}}{\partial x_k}) + \nu\left\langle\nabla^2\widetilde{u_i}\widetilde{u_k}\right\rangle\right]_T \quad (4)$$

The budgets of the double-averaged Reynolds shear stress are calculated using equation (5) for i =1 and k =3 and shown in figure 5. Similar to the dispersive shear stress, production (P), dissipation (ε) and convection (C) terms are negligible and not shown here and the main contribution to T is provided by pressure transport. Unlike the dispersive shear stress, large PSC and T terms are not confined in the area below the bar crest in flow over $\lambda/k = 5.2$. In this geometry, large contribution of PSC and T in the generation of $\langle u'w'\rangle^+$ are focused near the bed and bar crest and slight undulations of water surface has small contribution to that. In flow over $\lambda/k = 10.4$, the distribution of PSC is different than that in figure 4(b). The local large value of PSC at the bar crest extends to the bed in this case and a strong positive contribution of PSC is localized under the surface wave. The local maxima of T under the surface wave and at the downstream of bar crest are connected and extended to bed in figure 5(d) representing the interaction of

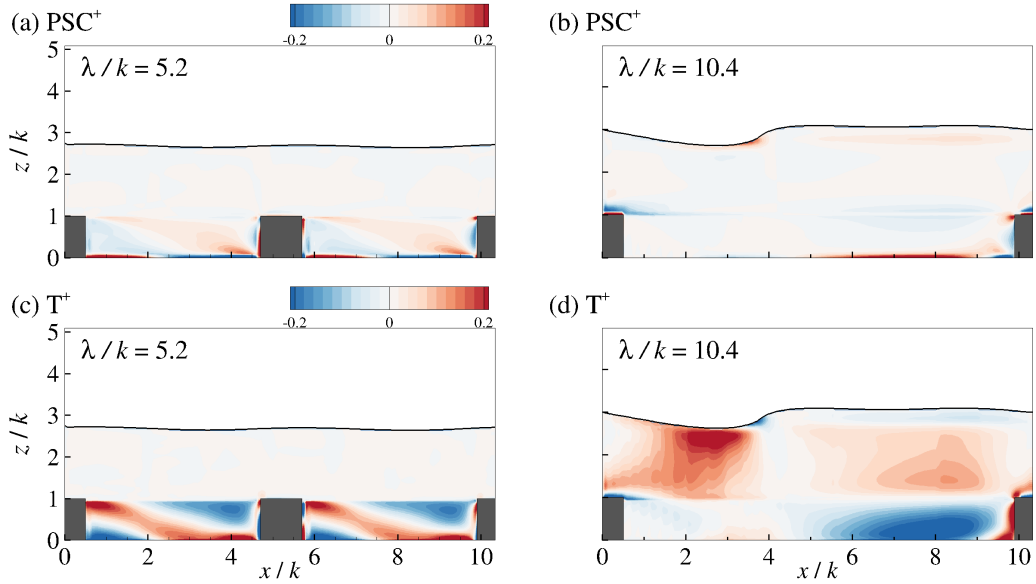

Figure 4. Dominant terms of dispersive shear stress budget for (a,c) $\lambda/k = 5.2$ and (b,d) $\lambda/k = 10.4$.

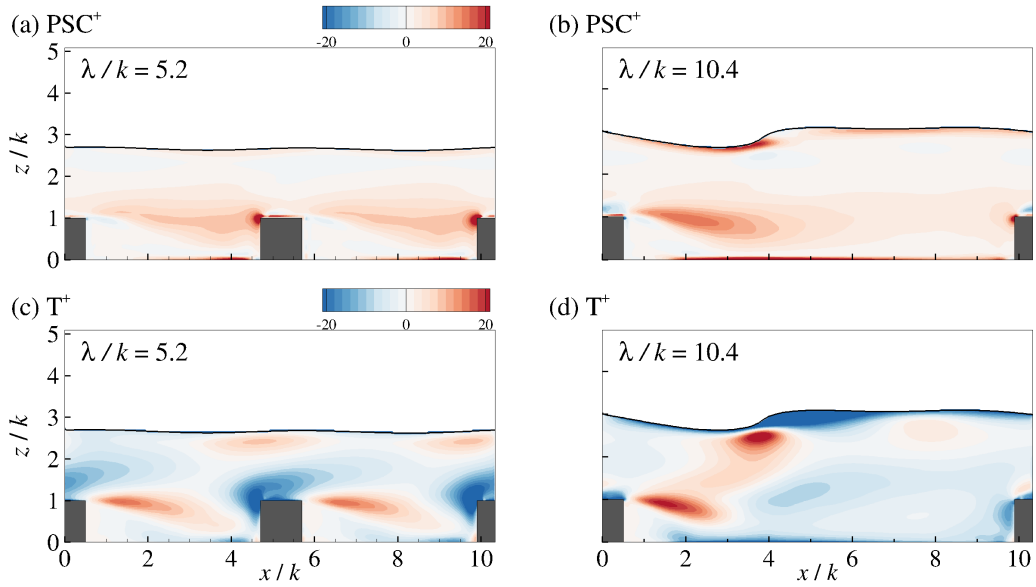

Figure 5. Dominant terms of double-averaged Reynolds shear stress budget for (a,c) $\lambda/k = 5.2$ and (b,d) $\lambda/k = 10.4$.

water surface, bar and bed in the transport of double-averaged Reynolds shear stress. To sum, as the large changes in spatial fluctuations of mean pressure and velocity occur under the bar crest, there is clear distinction in the distribution of dominant terms of $\langle\widetilde{u}\widetilde{w}\rangle^+$ under and above bar crest in both cases while in flow over larger bar spacing the effects of water surface leads to larger transport of dispersive shear stress in the bulk flow. The dominant term in budget of $\langle u'w'\rangle^+$ are strong near the bed and bar crest in flow over $\lambda/k = 5.2$ while in larger bar spacing the water surface contributes to the increase of PSC and T and the larger interaction of bed, bar and water surface enhances pressure transport in bulk flow in this case.

$$\frac{\partial < \overline{u_i'u_k'} >}{\partial t} = \left[-\langle\overline{u_j}\rangle \frac{\partial < \overline{u_i'u_k'} >}{\partial x_j} \right]_C + \left[- < \overline{u_k'u_j'} > \frac{\partial \langle\overline{u_i}\rangle}{\partial x_j} - < \overline{u_i'u_j'} > \frac{\partial \langle\overline{u_k}\rangle}{\partial x_j} - < \widetilde{u_i'u_j'} \frac{\partial \widetilde{u_k}}{\partial x_j} > - < \widetilde{u_k'u_j'} \frac{\partial \widetilde{u_i}}{\partial x_j} > \right]_P$$

$$+ \left[-2\nu < \overline{\frac{\partial u_i'}{\partial x_j}\frac{\partial u_k'}{\partial x_j}} > \right]_\varepsilon + \left[\frac{1}{\rho}(< p' \overline{\frac{\partial u_k'}{\partial x_i}} + p' \overline{\frac{\partial u_i'}{\partial x_k}} >) \right]_{PSC} + \left[- \frac{\partial < \overline{u_j'u_j'u_k'} >}{\partial x_j} - < \overline{\frac{\partial \widetilde{u_j}\widetilde{u_i'u_k'}}{\partial x_j}} > - \frac{1}{\rho}(\frac{\partial < p'u_k' >}{\partial x_i} + \frac{\partial < p'u_i' >}{\partial x_k}) + \nu < \nabla^2 \overline{u_i'u_k'} > \right]_T \quad (5)$$

Wake and Double-Averaged Turbulent Kinetic Energy Budget

The dominant terms contributing to the generation of wake and double-averaged turbulent kinetic energy ($1/2 < \widetilde{u_i}\widetilde{u_i} >$ and $1/2 < \overline{u_i'u_i'} >$) are production (P), transport (T) and convection (C) terms (equations 6 and 7). Figure 6(a,c,e) shows that the main contributors to the generation of WKE are negligible everywhere except under the bar in flow over $\lambda/k = 5.2$ which is consistent with figure 2(e). The large WKE for flow over $\lambda/k = 10.4$ is supplied by the convection term so

WKE is mainly generated by the interaction of water surface, bar and bed which leads to the larger spatial fluctuations of flow variables. The dominant term contributing to transport term in both geometries is the first term in T in equation 6 and is named here as dispersive transport. It is similar to turbulent transport (first term in T in equation 7) and large over the bar crest and under the water surface in flow over *k*-type roughness.

$$\frac{\partial <\widetilde{u_i}\widetilde{u_i}>}{\partial t} = \left[-\frac{1}{2}\left\langle\overline{u_j}\right\rangle \frac{\partial <\widetilde{u_i}\widetilde{u_i}>}{\partial x_j}\right]_C + \left[-<\widetilde{u_i}\widetilde{u_j}>\frac{\partial\langle\overline{u_i}\rangle}{\partial x_j} + <\widetilde{u_i'u_j'}\frac{\partial\widetilde{u_i}}{\partial x_j}>\right]_P + \left[-\nu<\frac{\partial\widetilde{u_i}}{\partial x_j}\frac{\partial\widetilde{u_i}}{\partial x_j}>\right]_\varepsilon + \left[-\frac{1}{2}\frac{\partial <\widetilde{u_i}\widetilde{u_i}\widetilde{u_j}>}{\partial x_j} - <\frac{\partial\widetilde{u_i'u_j'}\widetilde{u_i}}{\partial x_j}> - \frac{1}{\rho}(\frac{\partial\widetilde{p}\widetilde{u_i}}{\partial x_i}) + \frac{1}{2}\nu\left\langle\nabla^2\widetilde{u_i}\widetilde{u_i}\right\rangle\right]_T \quad (6)$$

$$\frac{\partial <\overline{u_i'u_i'}>}{\partial t} = \left[-\frac{1}{2}\left\langle\overline{u_j}\right\rangle \frac{\partial <\overline{u_i'u_i'}>}{\partial x_j}\right]_C + \left[-<\overline{u_i'u_j'}>\frac{\partial\langle\overline{u_i}\rangle}{\partial x_j} - <\widetilde{u_i'u_j'}\frac{\partial\widetilde{u_i}}{\partial x_j}>\right]_P + \left[-\nu<\overline{\frac{\partial u_i'}{\partial x_j}\frac{\partial u_i'}{\partial x_j}}>\right]_\varepsilon + \left[-\frac{1}{2}\frac{\partial <\overline{u_i'u_i'u_j'}>}{\partial x_j} - <\frac{1}{2}\frac{\partial\widetilde{u_j}\widetilde{u_i'u_i'}}{\partial x_j}> - \frac{1}{\rho}(\frac{\partial <p'u_i'>}{\partial x_j}) + \nu<\nabla^2\overline{u_i'u_i'}>\right]_T \quad (7)$$

The main source for production of the double-averaged turbulent kinetic energy are the bars (figure 7(a,b)) while the large deformation of the water surface contribute to P in flow over larger bar spacing too. The main contribution to the transport of $1/2<\overline{u_i'u_i'}>$ is turbulent transport and as seen in figure 7(d) standing wave over the water surface has a large contribution to its generation. This is consistent with figure 2(a-c). The large interaction of bed and water surface leads to the increase in the convection of double-averaged kinetic energy in figure 7(d). There is a large interaction between bar crest and standing wave in terms of negative convection and a large interaction between the reattachement area over the bed and upstream of the standing wave in terms of positive convection.

CONCLUSIONS

The results of large-eddy simulations of open channel flow over spanwise aligned square bars show the effects of roughness (bars) and water surface deformation on first and second order statistics. The large dispersive shear stress and wake kinetic energy in flow over larger bar spacing represents large interaction of bed and water surface in this case. Reynolds shear stress and turbulent kinetic energy are larger above the bar crest in flow over smaller bar spacing due to the presence of stable vortex between bars which skims the flow and limit the interaction of the flow under and above the bar crest. Quadrant analysis of Reynolds shear stress reveals the downward motion of fluid under the bar crest and its upward motion above this height. The non-negligible terms in dispersive and double-averaged Reynolds shear stress budgets are pressure-strain correlation and transport terms. The large contribution of the dominant terms to dispersive shear stress are visible only under the bar crest in flow over transitional roughness while the standing wave at the water surface over larger bar spacing enhances the contribution of these terms above the bar crest too. Pressure transport has the largest contribution to the generation of double-averaged Reynolds shear stress in both cases and it is affected by both bars and water surface. The dominant terms generating wake and double-averaged turbulent kinetic energy are production, transport and convection terms. The production term is mainly generated at the bar crest height while the convection term is large almost everywhere in the bulk flow.

ACKNOWLEDGEMENTS

Financial support was provided by the EPSRC/UK project "Rapid Monitoring of River Hydrodynamics and Morphology using Acoustic Holography", Grant No. EP/R022135/1.

REFERENCES

Djenidi, L., Elavarasan, R. & Antonia, R. A. 1999 The turbulent boundary layer over transverse square cavities. *Journal of Fluid Mechanics* **395**, 271–294.

Jalalabadi, R., Hwang, J., Nadeem, M., Yoon, M. & J., Sung H. 2017 Turbulent boundary layer over a divergent convergent superhydrophobic surface. *Physics of Fluids* **29**, 085112.

Jalalabadi, R. & Stoesser, T 2022*a* Large eddy simulation of free surface flow over square bars in laminar, transitional and turbulent flows. *39th IAHR World Congress* .

Jalalabadi, R. & Stoesser, T. 2022*b* Reynolds and dispersive shear stress in free-surface turbulent channel flow over square bars. *Physical Review E* **105**, 035102.

Jalalabadi, R., Stoesser, T., Ouro, P., Luo, Q. & Xie, Z. 2021 Level set methods for fluid interfaces. *Journal of Hydro-Environment Research* **36**, 64.

Jelly, T. O. & Busse, A. 2018 Reynolds and dispersive shear stress contributions above highly skewed roughness. *Journal of Fluid Mechanics* **852**, 710.

Jiminez, J 2004 The turbulent boundary layer over transverse square cavities. *Annual Review of Fluid Mechanics* **36(4)**, 173.

Kara, S., Kara, M. C., Stoesser, T. & Sturm, T. W. 2015 Free-surface versus rigid-lid LES computations for bridge-abutment flow. *Journal of Hydraulic Engineering* **141(9)**, 04015019.

McSherry, R., Chua, K., Stoesser, T. & Mulahasan, S. 2018 Free surface flow over square bars at intermediate relative submergence. *Journal of Hydraulic Research* **56(6)**, 825.

Nicoud, F. & Ducros, F. 1999 Subgrid-scale stress modelling based on the square of the velocity gradient tensor. *Flow Turbulence Combustion* **62(3)**, 183.

Raupach, M.R. & Shaw, R.H. 1982 Averaging procedures for flow within vegetation canopies. *Boundary-Layer Meteorology* **22(1)**, 79–90.

Sethian, J. A. & Smereka, P. 2003 Level set methods for fluid interfaces. *Annual Review of Fluid Mechanics* **35**, 146.

Wallace, J. M. 2016 Quadrant analysis in turbulence research: history and evolution. *Annual Review of Fluid Mechanics* **131**, 131.

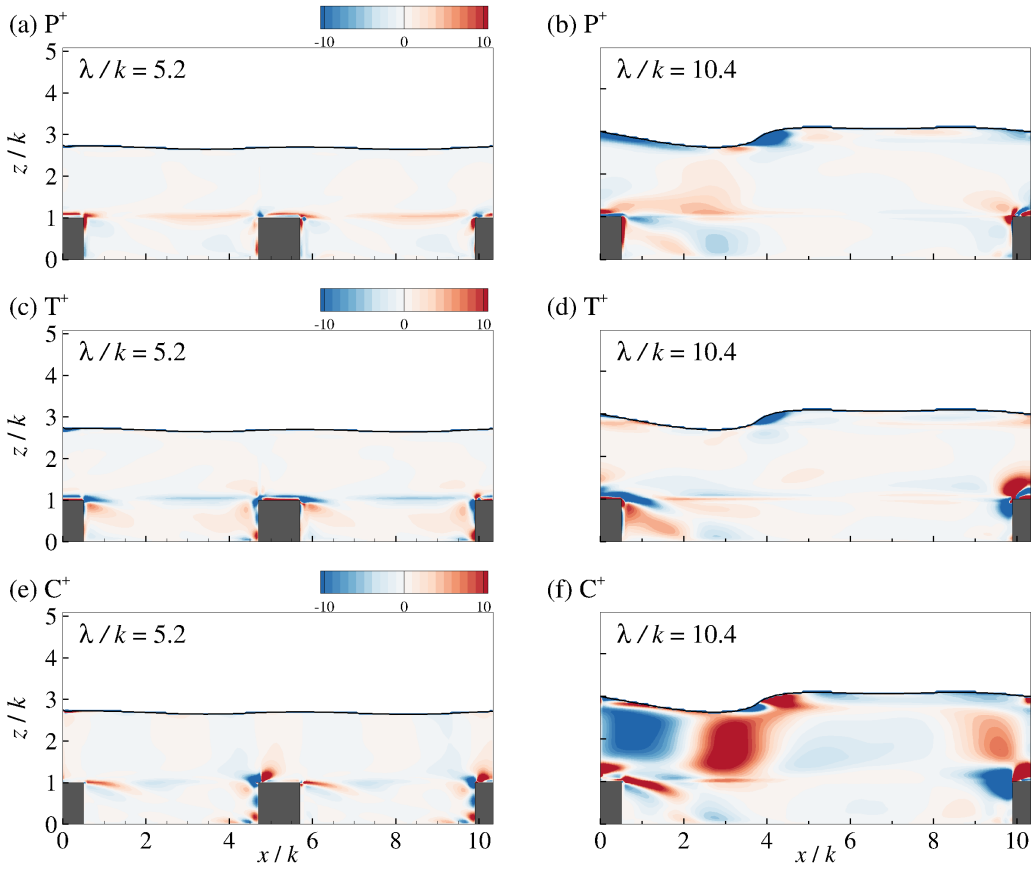

Figure 6. Dominant terms of wake kinetic energy budget for (a,c,e) $\lambda/k = 5.2$ and (b,d,f) $\lambda/k = 10.4$.

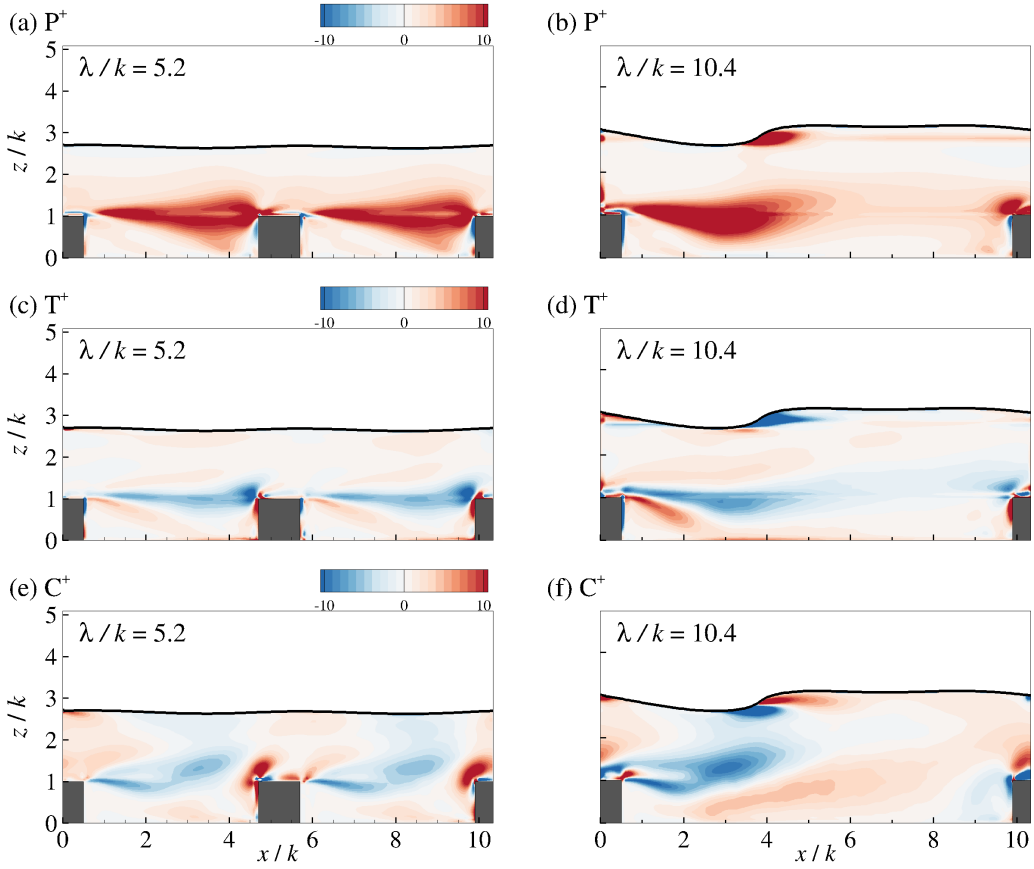

Figure 7. Dominant terms of turbulent kinetic energy budget for (a,c,e) $\lambda/k = 5.2$ and (b,d,f) $\lambda/k = 10.4$.